Calponin-Homology Domain mediated bending of membrane associated actin filaments

Saravanan Palani, Mohan K. Balasubramanian*, and Darius V. Köster*

Centre for Mechanochemical Cell Biology and Warwick Medical School, Division of Biomedical Sciences, CV4 7AL Coventry, UK
* Corresponding authors: M.K.Balasubramanian@warwick.ac.uk, D.Koester@warwick.ac.uk

Actin filaments are central to numerous biological processes in all domains of life. Driven by the interplay with molecular motors, actin binding and actin modulating proteins, the actin cytoskeleton exhibits a variety of geometries. This includes structures with a curved geometry such as axon-stabilizing actin rings, actin cages around mitochondria and the cytokinetic actomyosin ring, which are generally assumed to be formed by short linear filaments held together by actin cross-linkers. However, whether individual actin filaments in these structures could be curved and how they may assume a curved geometry remains unknown. Here, we show that "curly", a region from the IQGAP family of proteins from three different organisms, comprising the actin-binding calponin-homology domain and a C-terminal unstructured domain, stabilizes individual actin filaments in a curved geometry when anchored to lipid membranes. Whereas F-actin is semi-flexible with a persistence length of ~10 μm, binding of mobile curly within lipid membranes generates actin filament arcs and full rings of high curvature with radii below 1 μm. Higher rates of fully formed actin rings are observed in the presence of the actin-binding coiled-coil protein tropomyosin, and also when actin is directly polymerized on lipid membranes decorated with curly. Strikingly, curly induced actin filament rings contract upon the addition of muscle myosin II filaments and expression of curly in mammalian cells leads to highly curved actin structures in the cytoskeleton. Taken together, our work identifies a new mechanism to generate highly curved actin filaments, which opens a new range of possibilities to control actin filament geometries, that can be used, for example, in designing synthetic cytoskeletal structures.

The IQGAP family of proteins plays a key role in actin cytoskeleton regulation including the assembly and function of the contractile actomyosin ring in budding and fission yeasts (Briggs & Sacks, 2003; Eng et al., 1998; Epp & Chant, 1997; Tebbs et al., 2013). To study the mechanism and role of actin binding by the fission yeast IQGAP (encoded by the *rng2* gene), we utilized a strategy to investigate its function when immobilized on supported lipid bilayers. We chose this approach, since during cytokinesis Rng2, which binds a number of actomyosin ring proteins, is tethered to the plasma membrane via Mid1 ensuring the formation and anchoring of the cytokinetic ring (Laplante et al., 2016; Laporte et al., 2011; Padmanabhan et al., 2011). We linked hexa-histidine tagged *rng2* protein fragments to supported lipid bilayers containing nickel-chelating lipids (DOGS-NTA(Ni^{2+})) and observed the binding of fluorescently labelled actin filaments using live total internal reflection fluorescence (TIRF) microscopy as described earlier (Köster et al., 2016) (Figure 1A). The actin-binding calponin homology domain (CHD) is located at the N-terminus of Rng2 (AA 41-147), and the construct His$_6$-Rng2[1-189] (subsequently referred to as curly) containing the CHD and additional 42 amino acids was found to bind actin filaments (Figure 1B, Figure 1-figure supplement 1A-C). Remarkably, when bound to His$_6$-Curly a large fraction of actin filaments formed tightly bent rings (21 ± 5 rings per field of view) with a characteristic curvature C_{curly} = 1.7 ± 0.5 μm^{-1} (N = 425) (Figure 1 C; Figure 1 – figure supplement 1 D; Video 1). To our knowledge, this is an unprecedented phenomenon specific to curly. Binding of other membrane attached actin binding proteins in the same geometry does not appreciably bend actin ($C_{\alpha\text{-actinin}}$ = 0.3 ± 0.1 μm^{-1}, N = 85; $C_{EzrinABD}$ = 0.5 ± 0.3 μm^{-1}, N = 127) (Figure 1-figure supplement 2 A-D). Membrane anchored fimbrin has also been shown not to bend actin (Murrell & Gardel, 2012).
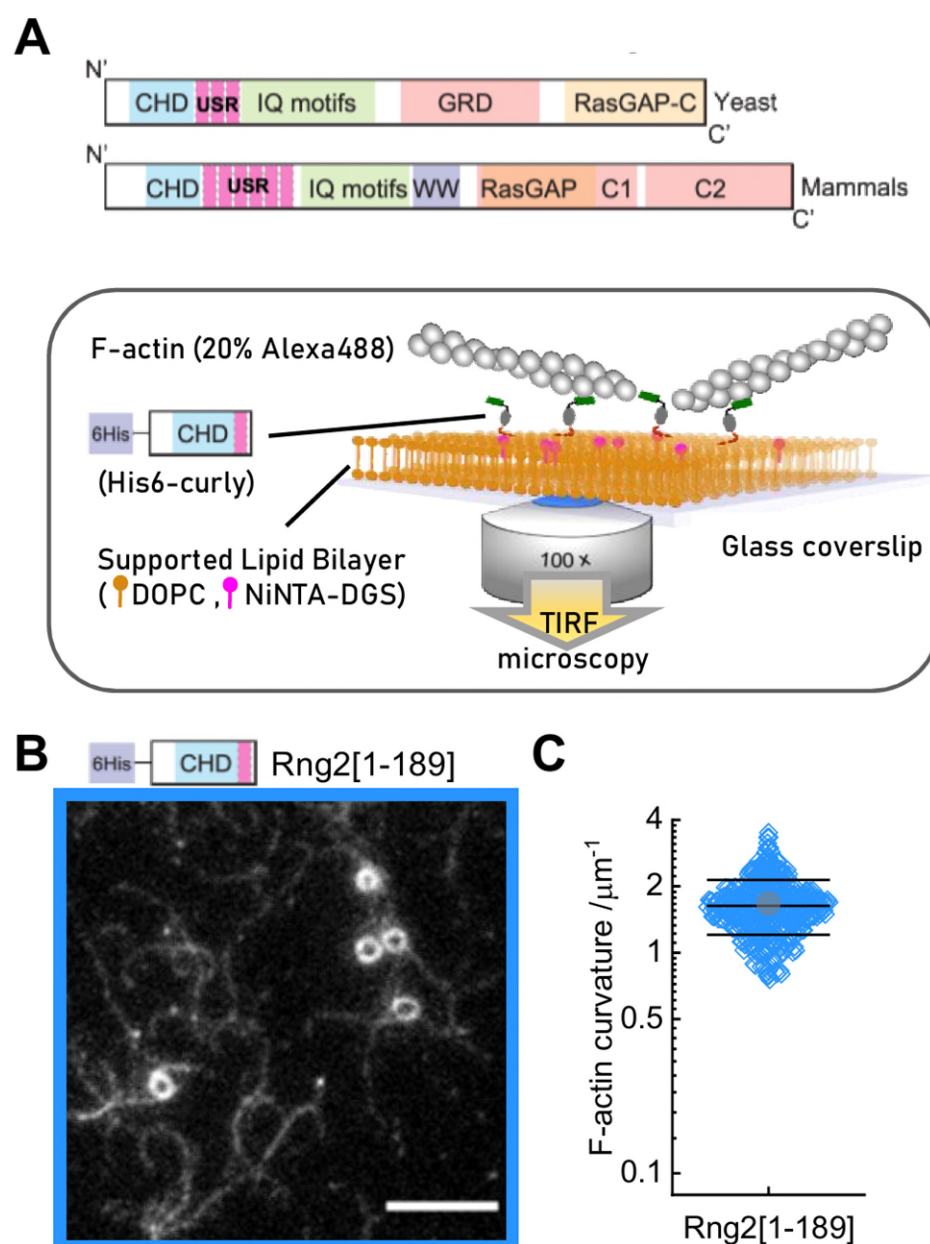
60

Figure 1

61
62 **Figure 1 – Formation of actin filament rings by membrane tethered curly (Rng2[1-189])**
63   (A) Schematic representation of (top) the IQGAP proteins Rng2 (yeast, *S. pombe*) and
64   IQGAP1 (mammals, *H. Sapiens*) and (bottom) the experimental setup used in this study;
65   CHD - Calponin Homology Domain, USR – Unstructured Region, GRD - GAP Related
66   Domain, RasGAP – Ras GTPase Activating Protein, WW – tryptophan containing protein
67   domain.
68   (B) TIRF microscopy image of actin filaments (Alexa488) bound to SLB tethered His_6-curly;
69   scale bar 5 μm.
70   (C) Curvature measurements of actin filament rings and curved segments; shown are the
71   individual data points and their mean ± s.d.; N = 425 obtained from 8 field of views from
72   4 individual experiments.
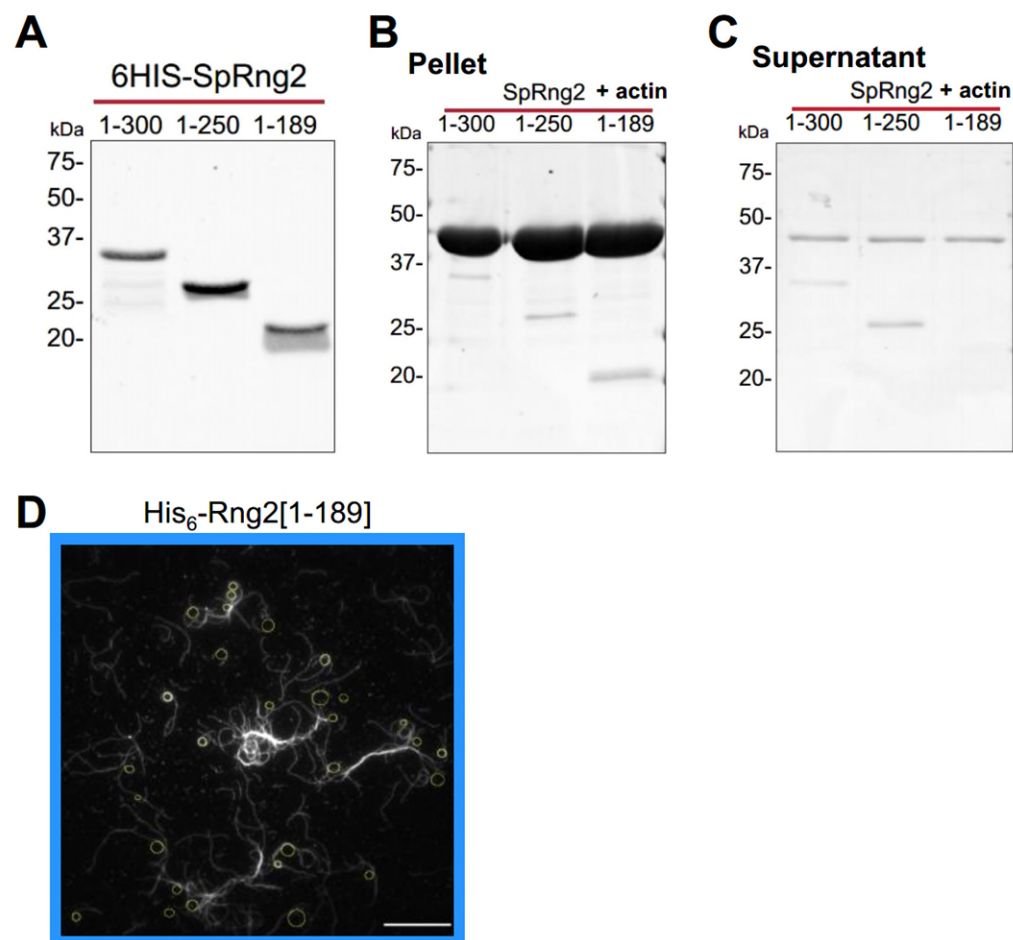
73
74

Figure 1 - figure supplement 1

Figure 1 – figure supplement 1

(A) Western blot of the different His_6-Rng2 constructs after protein purification.

(B) SDS-PAGE of the actin filament pellet after incubation with His_6-Rng2 constructs and centrifugation at 100,000g for 20 min at 25°C.

(C) SDS-PAGE of the supernatant from the sample described in (B).

(D) TIRF microscopy image of actin filaments (Alexa488) bound to SLB tethered His_6- curly; circles show curvature measurements; scale bar 10 μm.
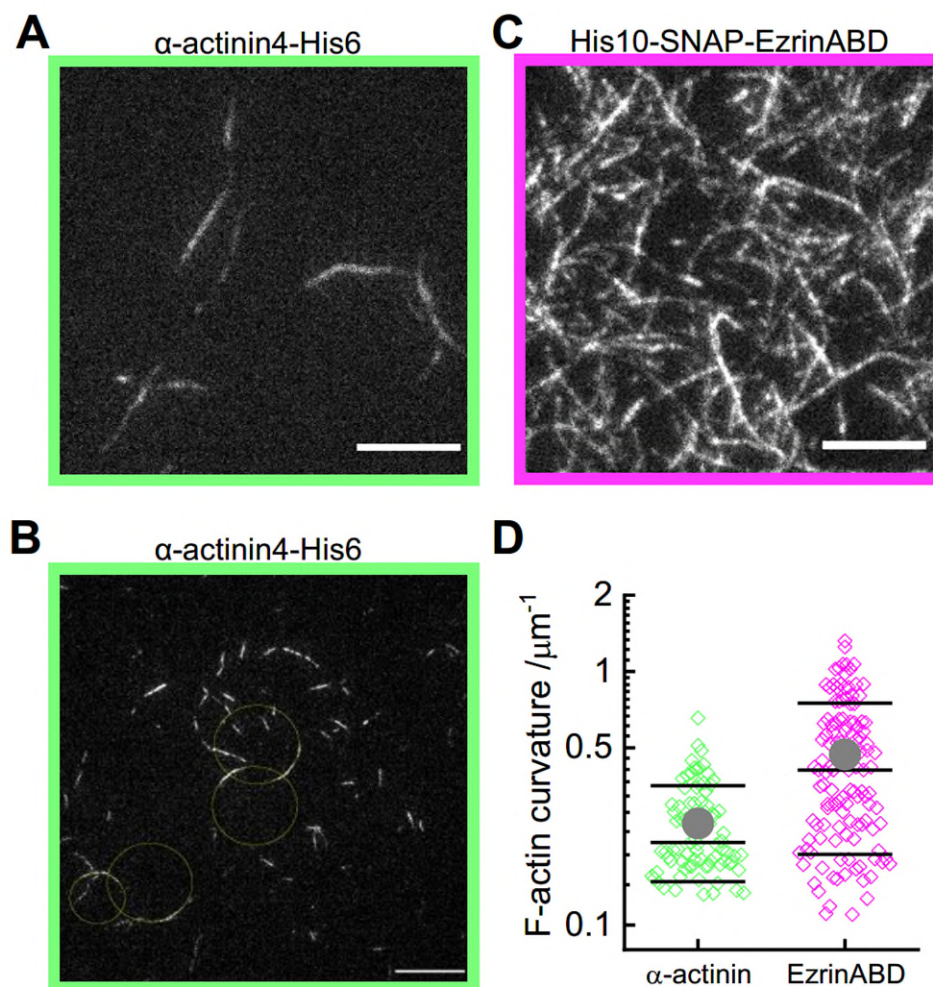
Figure 1 - figure supplement 2

A α-actinin4-His6

C His10-SNAP-EzrinABD

B α-actinin4-His6

D

Figure 1-figure supplement 2

(A) TIRF microscopy image of actin filaments (Alexa488) bound to SLB tethered α-actinin-His_6; scale bar 5 µm.

(B) TIRF microscopy image of actin filaments (Alexa488) bound to SLB tethered α-actinin-His_6; circles show curvature measurements; scale bar 10 µm.

(C) TIRF microscopy image of actin filaments (Alexa488) bound to SLB tethered His_{10}-EzrinABD; scale bar 5 µm.

(D) Curvature measurements of actin filament rings and curved segments; shown are the individual data points and their mean ± s.d.; α-actinin-His_6: N = 85 obtained from 10 field of views from 4 individual experiments; His_{10}-EzrinABD : N = 127 obtained from 9 field of views from 3 individual experiments.

4

120   To understand the mechanism leading to actin filament bending and ring formation by curly,
121   we tested the role of different fragments of curly and their orientation as well as curly
122   anchoring to lipid membranes in actin filament bending. Curly mobility within planar lipid
123   membranes was important for actin bending as glass adsorbed, immobilized His_6-Curly
124   displayed reduced actin bending and ring formation ($C_{glass} = 0.6 \pm 0.3$ µm^{-1}, N = 138) (Figure
125   2 A, F), and when using membrane tethered fluorescently labelled His_6-SNAP-curly, a weak
126   accumulation of curly under actin filaments could be observed (Figure 2- figure supplement
127   1). Next, we generated fragments of curly to discern the regions important for actin binding
128   and bending. We found that the C-terminal region following the CHD (His6-Rng2[150-250])
129   alone was able to bind actin filaments without inducing bending ($C_{[150-250]} = 0.2 \pm 0.1$ µm^{-1}, N
130   = 17) (Figure 2 B). Interestingly, a 7AA deletion (Rng2[1-189]-Δ(154-160)) led to a reduced
131   degree of actin binding and bending ($C_{\Delta(154-160)} = 0.4 \pm 0.1$ µm^{-1}, N = 33) (Figure 2 C).
132   Similarly, the fragments Rng2[41-189] and Rng2[1-147] displayed weaker actin binding and
133   bending compared to curly ($C_{[41-189]} = 0.6 \pm 0.2$ µm^{-1}, N = 323; $C_{[1-147]} = 0.7 \pm 0.2$ µm^{-1}, N =
134   118) (Figure 2 D, E). The location of the hexa-histidine tag to link curly to the lipid membrane
135   (C-terminal hexa-histidine tagged construct Rng2[1-189]-His_6) did not affect actin filament
136   bending (25 ± 7 rings per field of view; $C_{curly-his} = 1.5 \pm 0.5$ µm^{-1}, N = 184) (Figure 2 F). Taken
137   together (Figure 2 G), this suggests that curly contains two actin binding sites, one located
138   within the CHD followed by a second within Rng2[148-189]. Both actin binding sites are
139   necessary for actin bending as neither Rng2[1-147] nor Rng2[150-250] caused strong
140   bending. It is very likely that the second actin binding site includes the 7AA Rng2[154-160]
141   as this unstructured region maps directly to AA 240-246 of the dystrophin CH2 domain
142   (Wang et al., 2004). The first 40 AA of Rng2 are likely to be important for the protein folding
143   and stability, because of which the Rng2[41-189] construct showed poor actin binding and
144   did not lead to actin bending.
145
146
147
148
149
150
151
152
153
154
155
156
157
158
159
160
161
162
163
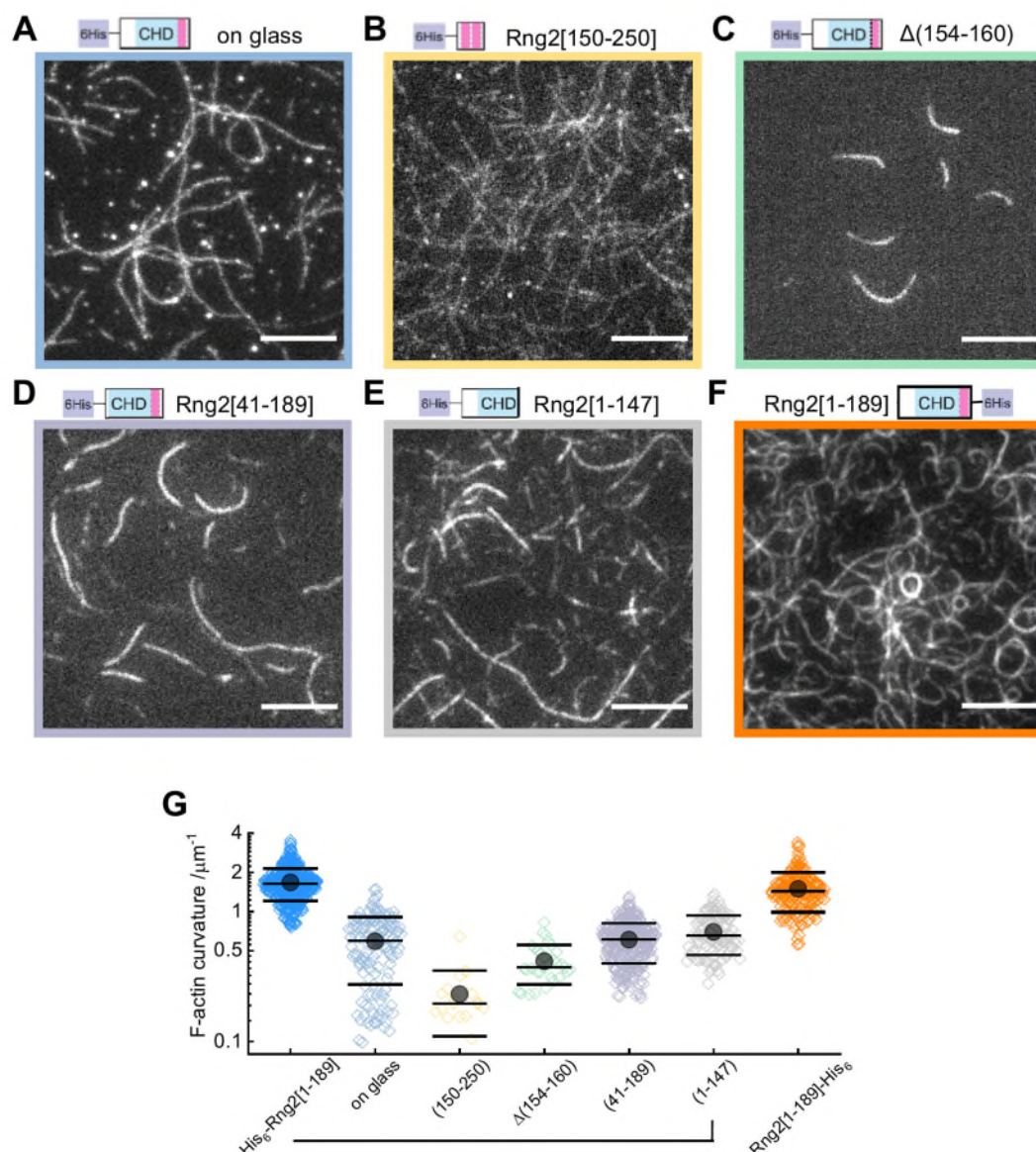164

165

Figure 2

Figure 2 – Characterization of actin binding and bending by fragments of curly

TIRF microscopy images of actin filaments (Alexa488) bound to

    (A) glass adsorbed His6-curly; N = 138 from 9 field of views from 3 independent experiments;

    (B) SLB bound His$_6$-Rng2[150-250]; N = 144 from 10 field of views from 2 independent experiments;

    (C) SLB bound His$_6$-Rng2[1-189]Δ(154-160); N = 33 from 10 field of views from 2 independent experiments;

    (D) SLB bound His$_6$-Rng2[41-189]; N = 323 from 9 field of views from 3 independent experiments;

    (E) SLB bound His$_6$-Rng2[1-147]; N = 118 from 12 field of views from 2 experiments;

    (F) SLB bound Rng2[1-189]-His$_6$; N = 658 from 16 field of views from 4 experiments; Scale bars: 5 μm.

    (G) Curvature measurements of actin filament rings and curved segments; shown are the individual data points and their mean ± s.d.
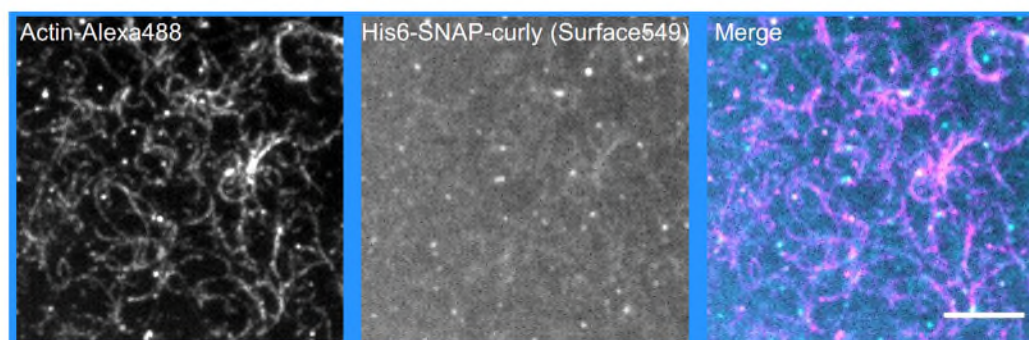
6

Figure 2 - figure supplement 1

184
185 **Figure 2- supplement figure 1**
186   Dual color TIRF microscopy image of actin filaments (Alexa488, magenta) bound to SLB
187   tethered fluorescently labelled His$_6$-SNAP-curly (Surface549, cyan); scale bar 5 μm.
188
189
190
191
192
193
194
195
196
197
198
199
200
201
202
203
204
205
206
207
208
209
210
211
212
213
214
215
216
217
218
219
220
221
222
223
224
225

7

226   Careful examination of individual actin filaments bound to membrane tethered His$_6$-Curly
227   allowed us to identify the occurrence of discrete kinks of an angle $\alpha = 37° \pm 8°$ (N = 63) along
228   actin filaments during the transition from straight to bent filaments (Figure 2-figure
229   supplement 2 A, B; Video 2). Based on the experimental data and the predicted molecular
230   structure of curly (Rng2[1-189]) we hypothesize that i) the CHD (Rng2[41-147]) contains at
231   least one actin binding site (similar to the utrophin actin binding domains ABD2' (UTRN[84-
232   94]) and ABD2 (UTRN[107-126]) (Kumari et al., 2020)) and ii) the C-terminal extension from
233   the CHD contains an additional actin binding site (including Rng2[154-160]) (Wang et al.,
234   2004). The latter could lead to a change in the actin subunit orientation within the actin
235   filament similar to the action of cofilin (Narita, 2020) and could lead to overall actin bending
236   when the binding is asymmetric (Figure 2-figure supplement 2 C). However, in contrast to
237   cofilin, we could not observe any events actin filament severing by curly.
238
239
240
241
242
243
244
245
246
247
248
249
250
251
252
253
254
255
256
257
258
259
260
261
262
263
264
265
266
267
268
269
270
271
272
273
274
275
276
277
278
279
280
281
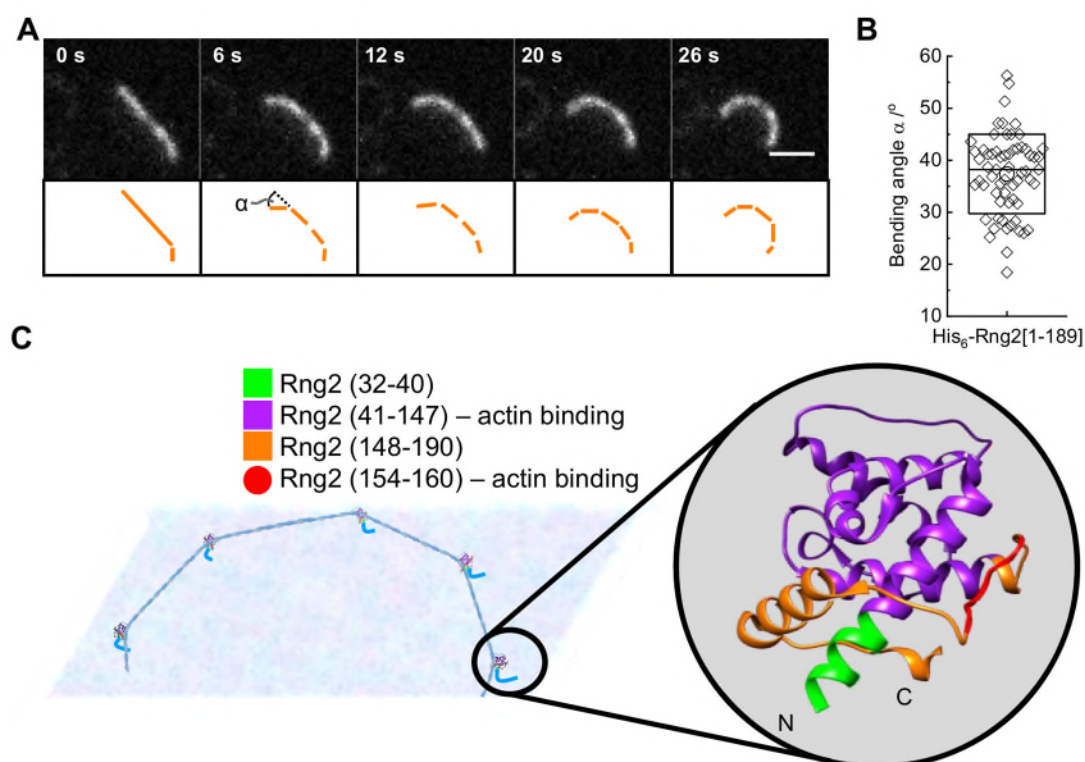282
283

Figure 2 - figure supplement 2

Figure 2- supplement figure 2

    (A) TIRF microscopy image time series of an actin filament (Alexa488) bound to SLB tethered His_6-curly and displaying stepwise bending; scale bar: 1 µm.

    (B) Bending angles of individual bending events in actin filaments; shown are the individual data points and their mean ± s.d.; N = 63 from 6 individual actin filaments.

    (C) Model representation of curly and how it could interact with actin to induce local bends in the actin filament; the inlet shows curly with the regions tested in this study highlighted in color.

317 Next, we studied whether actin bending by curly depended on the orientation of actin
318 filaments by following the landing of actin filaments decorated with labelled capping protein
319 as a plus end marker (Bieling et al., 2016). We found that the bending was oriented anti-
320 clockwise with respect to the plus end in all instances where the plus end was clearly
321 labelled and the orientation of filament bending could be identified (Figure 3A, B; Figure 3-
322 figure supplement 1 A, B). This was observed using both, the N-terminal and C-terminal
323 hexa-histidine tagged curly indicating that the internal sequence of the two actin binding
324 sites within curly sets the chirality of actin bending and not the position of the membrane
325 linker (Figure 3A, B; Figure 3-figure supplement 1 A, B; Video 3, 4). Actin filaments
326 appeared to bend concomitant with their landing on the supported lipid bilayer, which
327 indicates that the bending did not require the full actin filament to be tethered to the SLB and
328 underlined the earlier observation that the bending occurred locally.

330 To decouple the actin filament bending from the landing of actin filaments, we induced
331 polymerization of actin filaments at planar lipid membranes in the presence of membrane
332 tethered curly (His$_6$-Curly) by using membrane tethered formin (His$_6$-SpCdc12(FH1-FH2)),
333 profilin-actin and ATP. Strikingly, polymerizing actin filaments displayed characteristic
334 bending shortly after the onset of polymerization and grew often into full rings (44 ± 6 rings
335 per field of view, $C_{formin\ rings}$ = 1.7 ± 0.4 µm^{-1}, N = 477; $C_{formin\ short}$ = 1.1 ± 0.3 µm^{-1}, N = 125)
336 (Figure 3 C, D; Figure 3-figure supplement 1 C, D; Video 5). By contrast, polymerization of
337 actin filaments along SLBs decorated with His$_{10}$-SNAP-EzrinABD did not result in the
338 formation of arcs and rings, establishing that actin filament bending was due to curly and not
339 due to formin (Figure 3-figure supplement 1 E, F). These observations showed that actin
340 bending occurs continuously due to the binding of membrane tethered curly and did not
341 require the cross-linking of adjacent ends of the same filament as was observed with the
342 actin cross-linker anillin (Kučera et al., 2020). Importantly, the uni-directional bending
343 supports the hypothesis that the binding site of curly with actin filaments defines an
344 orientation, and the propagation of a curved trajectory once established indicates a
345 cooperative process.

347 Actin filaments forming the cytokinetic ring in *S. pombe* are wrapped by the coiled-coil
348 protein tropomyosin (Cdc8), while the actin cross-linker fimbrin is present outside the
349 cytokinetic ring region in Arp2/3 generated actin patches and prevents tropomyosin of
350 binding to actin filaments in these patches (Skau & Kovar, 2010). To find out whether the
351 actin bending effect of curly is conserved in tropomyosin wrapped actin filaments, we
352 incubated actin filaments with tropomyosin before adding them to His$_6$-Curly containing
353 SLBs. Strikingly, addition of tropomyosin to actin filaments increased the frequency of actin
354 ring formation without affecting actin filament curvature (38 ± 3 rings per field of view;
355 $C_{tropomyosin}$ = 1.4 ± 0.6 µm^{-1}, N = 204), while actin filaments incubated with the actin cross-
356 linker fimbrin displayed reduced bending and ring formation (3 ± 2 rings per field of view;
357 $C_{fimbrin}$ = 0.6 ± 0.4 µm^{-1}, N = 407) (Figure 3-figure supplement 2 A-E; Video 6). Thus, the
358 tropomyosin Cdc8 and curly cooperate to enhance actin filament bending and ring formation.

360 Interestingly, we could observe that long actin filaments coated with tropomyosin would trace
361 consecutive rings around the same center while landing on curly decorated lipid
362 membranes. Subtraction of the image after completion of the first round of actin filament
363 landing into a ring from the image after the second round revealed that the second ring
364 occupied the interior space of the first ring. In line with that, comparison of the intensity
365 profiles perpendicular to the actin filament of the first and second round of ring formation
366 revealed a widening of the profile towards the interior of the ring (Figure 3-figure supplement
367 3 A, B). A similar effect could be observed in examples of actin filaments polymerized by
368 membrane tethered formin in the presence of membrane tethered curly (Figure 3-figure
369 supplement 3 C, D). This would suggest that curly can arrange long actin filaments into an
370 inward oriented spiral.

372 To test whether the curly-induced actin rings can contract, we added rabbit skeletal muscle
373 myosin II filaments and ATP to curly bound actin filaments and followed actin filament
374 dynamics over time. After the myosin II filaments landed on the actin filaments, straight actin

375 filaments were propelled by myosin action and eventually started to bend and displayed a
376 variety of dynamics including translation, rotation and finally contraction of actin rings (Figure
377 3 E, Figure 3-figure supplement 4 A, Video 7). Interestingly, most actin rings displayed a
378 counter-clockwise rotation (34/36 cases) and the contraction was slow with $v_{contraction}$ = 3 ±
379 0.7 nm s^{-1} (N = 29) (Figure 3 F; Video 8). Despite reaching high curvatures of C_{myoII} = 2.8 ±
380 0.7 μm^{-1} (N = 342) with a maximum of 6.3 μm^{-1} there was no evidence of breaking of actin
381 filaments during the contraction process (Figure 3 G). Additionally, the myosin II induced
382 flows of actin filaments increased the formation of actin rings significantly (79 ± 8 rings per
383 field of view) indicating that myosin II filament induced actin filament sliding enhanced the
384 ability of membrane anchored curly to generate actin filament bending (Figure 3-figure
385 supplement 4 B, C). In line with this, actin filament rings displayed increased localization of
386 fluorescently labelled curly after addition of myosin II filaments action indicating that curly
387 showed an increased affinity for highly bent actin and/ or stabilized actin filaments at higher
388 curvatures (Figure 3-figure supplement 4 D). Interestingly, despite the observed high
389 curvatures of actin filaments upon myosin II filament action, severing of actin filament was
390 not observed suggesting that binding of curly reduces the rigidity of actin filaments.
391
392 It was not obvious that addition of myosin II filaments would lead to actin ring constriction
393 without the addition of any cross-linkers or other factors. When taking into account that curly
394 arranges actin filaments into an inward spiral, a possible explanation for actin ring
395 constriction would be that the myosin II filament acts both as a cross-linker and motor
396 protein: one end of the myosin II filament sits at the actin filament plus end while other
397 myosin head domains of the same myosin II filament pull along the same actin filament to
398 travel towards the plus end leading to constriction (Figure 3-figure supplement 4 E). This
399 would result in sub-optimal myosin head orientations towards the actin filament, which could
400 explain the observed slow constriction rates that were orders of magnitude slower than the
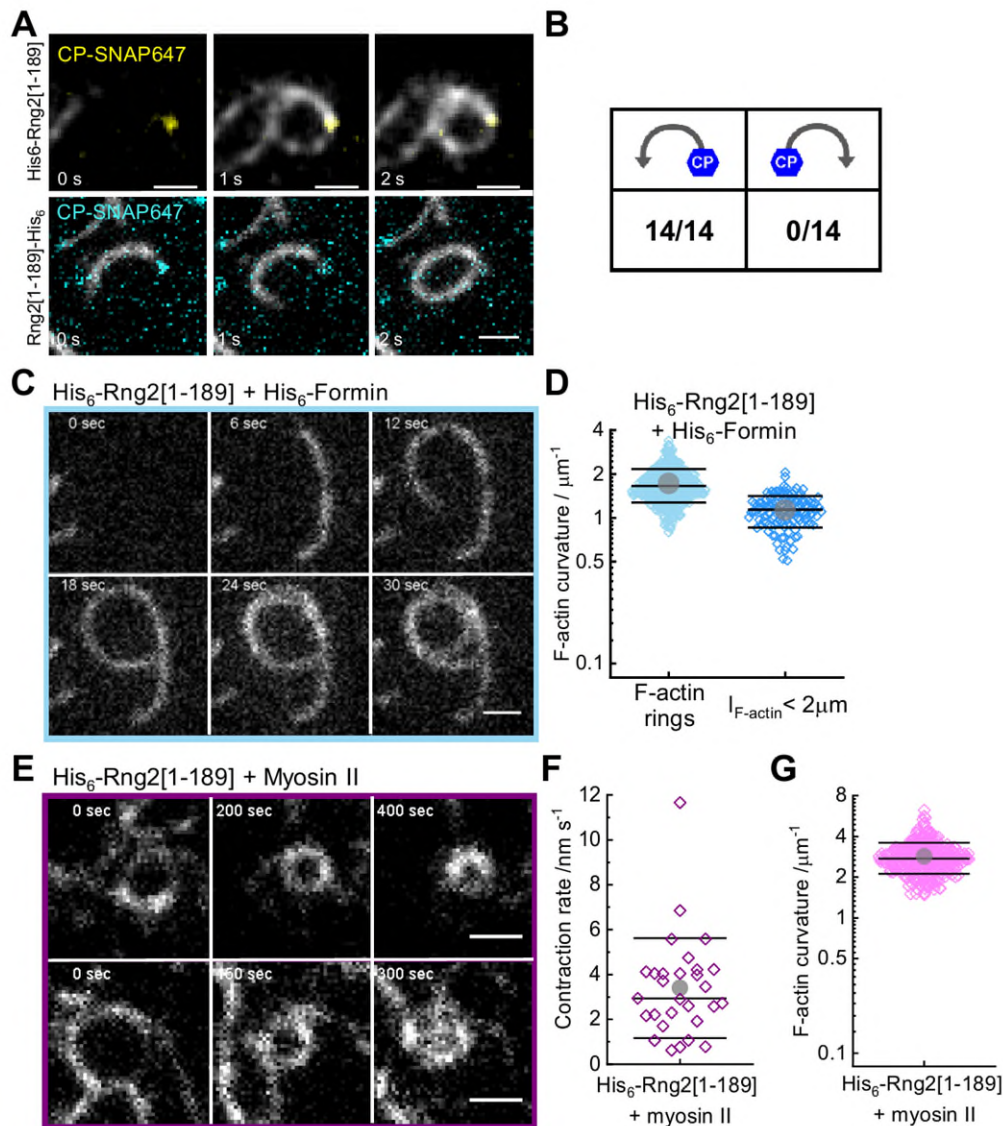401 reported values for actin propulsion by myosin II in motility assays (Toyoshima et al., 1990).
402
403
404
405
406
407
408
409
410
411
412
413
414
415
416
417
418
419
420
421
422
423
424
425
426
427
428
429

Figure 3

430
431 **Figure 3 – Curly recognizes actin filament orientation and enables actin ring contraction**
432 **by myosin II**
433   (A) TIRF microscopy images of actin filaments (Alexa488) with the plus end marked with
434   SNAP647-tagged capping protein binding to His_6-curly (top) and curly-His_6 (bottom);
435   scale bar: 1 μm.
436   (B) Count of actin filament bending orientations with respect to the capping protein where
437   individual actin filaments could be identified.
438   (C) TIRF microscopy images of a polymerizing actin filament (Alexa488) driven by
439   membrane tethered His_6-formin in the presence of His_6-curly; scale bar: 1 μm.
440   (D) Curvature measurements of actin filament rings (light blue) and curved short actin
441   filaments (< 2 μm; dark blue); shown are the individual data points and their mean ±
442   s.d.; N_{rings} = 477, N_{short} = 125 from 9 field of views of 3 independent experiments.
443   (E) TIRF microscopy images of actin filament (Alexa488) ring contraction after addition of
444   muscle myosin II filaments on His_6-curly containing SLBs; scale bar: 1 μm.
445   (F) Average contraction rates of actin filament rings after addition of muscle myosin II
446   filaments; shown are the individual data points and their mean ± s.d.; N = 18 from 2
447   individual experiments.
448   (G) Curvature measurements of actin filament rings and curved segments 20 min after
449   addition of myosin II filaments; shown are the individual data points and their mean ±
450   s.d.; N = 342 from 10 field of views of 2 individual experiments.

12

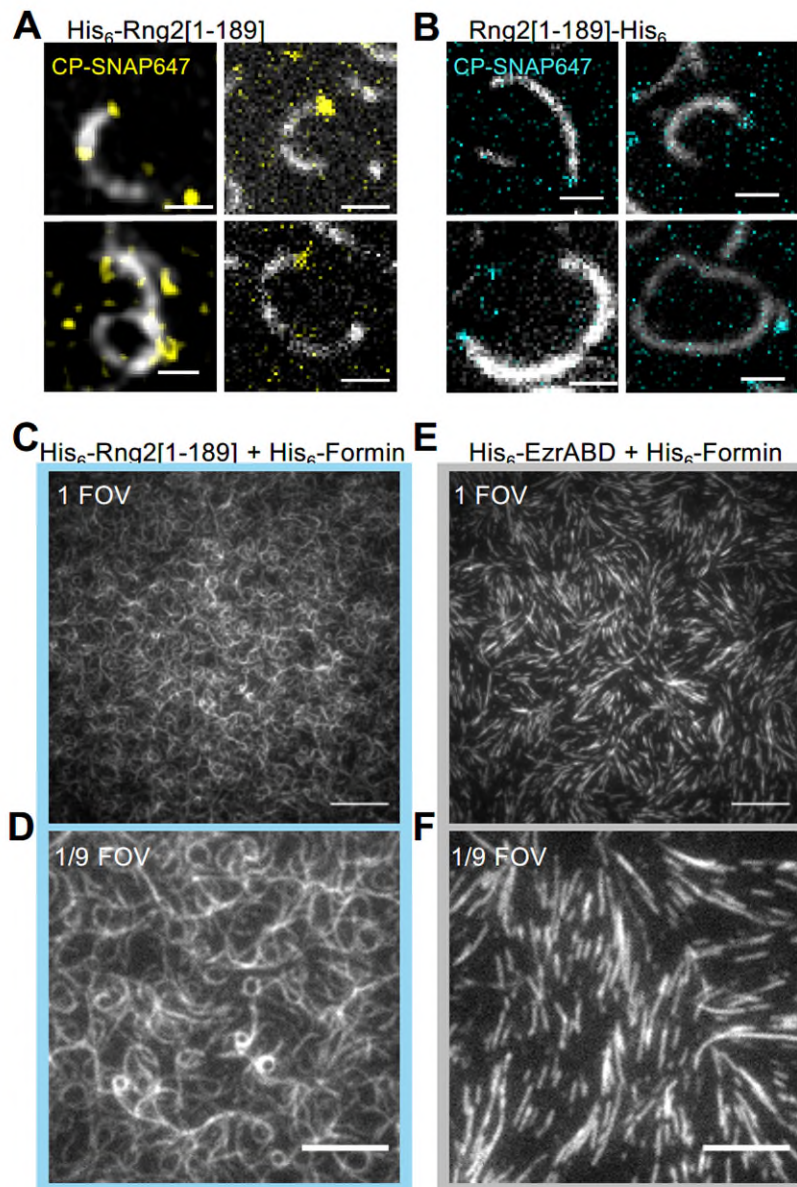# Figure 3 - figure supplement 1

451
452 **Figure 3-figure supplement 1**

(A) TIRF microscopy images of actin filaments (Alexa488) with the plus end marked with SNAP647-tagged capping protein binding to His_6-curly; scale bar: 1 µm.

(B) TIRF microscopy images of actin filaments (Alexa488) with the plus end marked with SNAP647-tagged capping protein binding to curly- His_6; scale bar: 1 µm.

(C) TIRF microscopy image (representing one field of view) of actin filaments (Alexa488) polymerized by membrane tethered His_6-formin in the presence of His_6-curly; scale bar: 10 µm.

(D) TIRF microscopy image (representing 1/9 of the field of view) of actin filaments (Alexa488) polymerized by membrane tethered His_6-formin in the presence of His_6-curly; scale bar: 5 µm.

(E) TIRF microscopy image (representing one field of view) of actin filaments (Alexa488) polymerized by membrane tethered His_6-formin in the presence of His_{10}-ErzinABD; scale bar: 10 µm.

(F) TIRF microscopy image (representing 1/9 of the field of view) of actin filaments (Alexa488) polymerized by membrane tethered His_6-formin in the presence of His_{10}-EzrinABD; scale bar: 5 µm.

469
470

13

Figure 3 - figure supplement 2
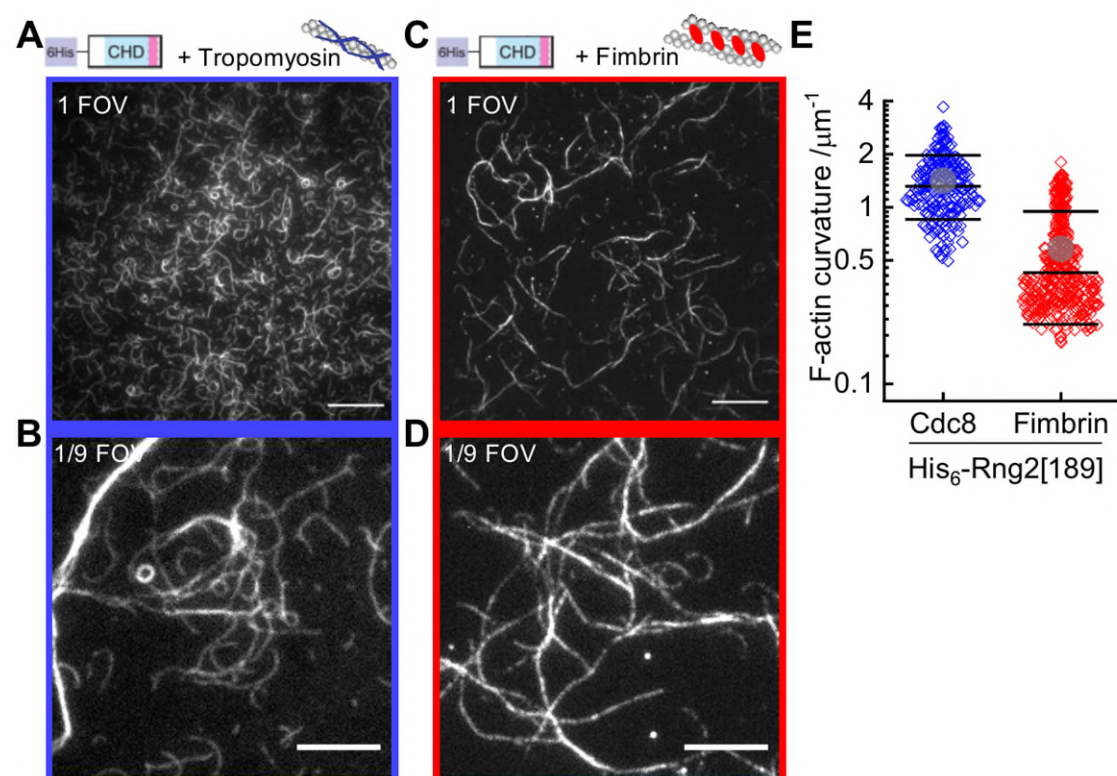

471
472
473 **Figure 3-figure supplement 2**
474   (A) TIRF microscopy image (representing one field of view) of actin filaments (Alexa488)
475   pre-incubated with tropomyosin (Cdc8) bound to membrane tethered His_6-curly; scale
476   bar: 10 μm.
477   (B) TIRF microscopy image (representing 1/9 field of view) of actin filaments (Alexa488)
478   pre-incubated with tropomyosin (Cdc8) bound to membrane tethered His_6-curly; scale
479   bar: 5 μm.
480   (C) TIRF microscopy image (representing one field of view) of actin filaments (Alexa488)
481   pre-incubated with fimbrin bound to membrane tethered His_6-curly; scale bar: 10 μm.
482   (D) TIRF microscopy image (representing 1/9 field of view) of actin filaments (Alexa488)
483   pre-incubated with fimbrin bound to membrane tethered His_6-curly; scale bar: 5 μm.
484   (E) Curvature measurements of actin filament rings and curved segments; shown are the
485   individual data points and their mean ± s.d.; tropomyosin (Cdc8, blue): N = 204 from 9
486   field of views of 3 individual experiments; fimbrin (red): N = 407 from 20 field of views
487   of 3 individual experiments.
488
489
490
491
492
493
494
495
496
497
498
499
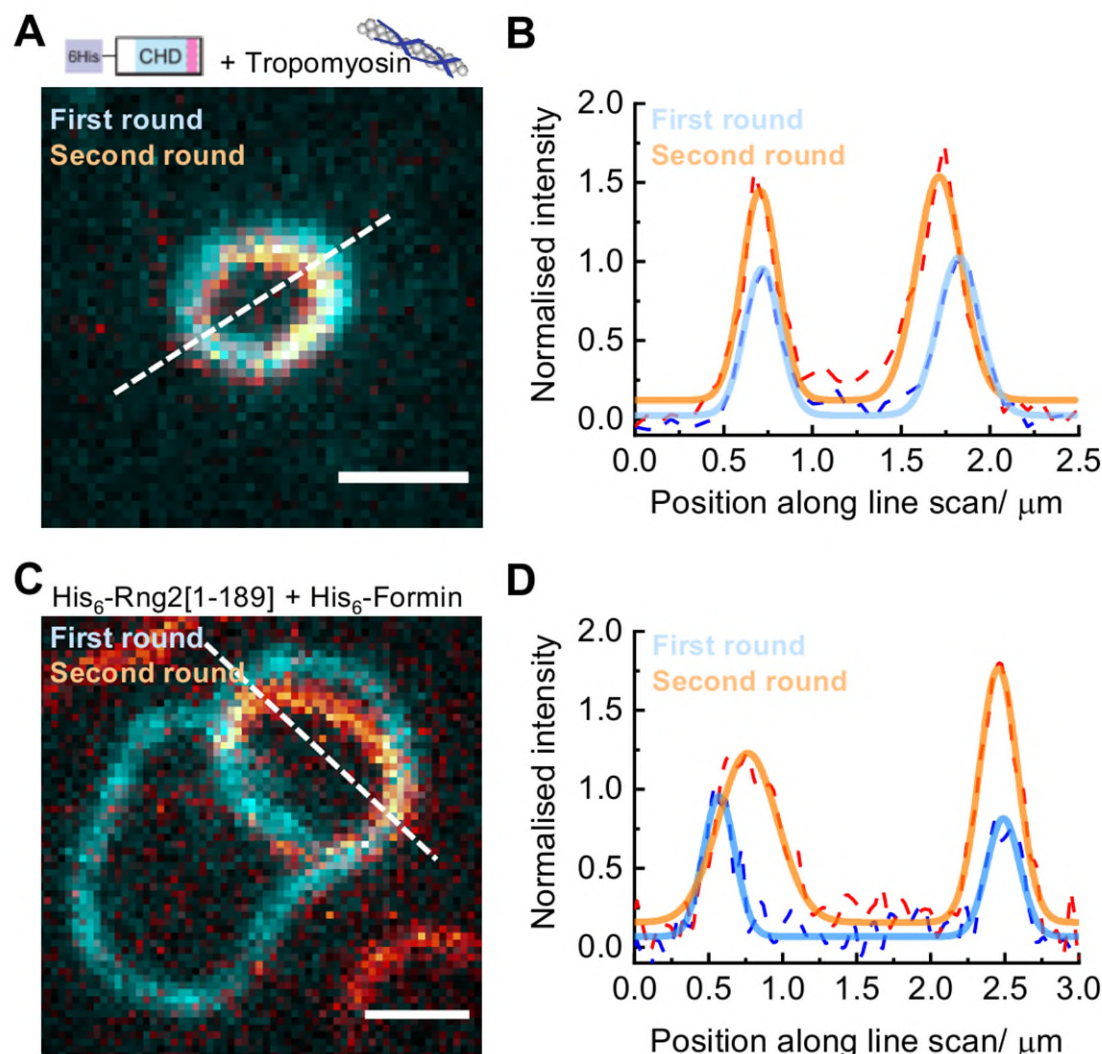500

14

Figure 3 - figure supplement 3

Figure 3-figure supplement 3

(A) TIRF microscopy image overlay showing multiple ring formation of a tropomyosin coated actin filament (Alexa488) during binding to membrane tethered His_6-curly; the first ring formed is colored in cyan, the second ring (in orange) was highlighted by subtracting the image of the first ring from the image stack; scale bar: 1 μm.

(B) Intensity line scan (3 pixels width) along the dashed line in (A) and corresponding Gaussian peak fits.

(C) TIRF microscopy image overlay showing multiple ring formation of a polymerizing actin filament (Alexa488) by membrane tethered His_6-formin in presence of membrane tethered His_6-curly; the first ring formed is colored in cyan, the second ring (in orange) was highlighted by subtracting the image of the first ring from the image stack; scale bar: 1 μm.

(D) Intensity line scan (3 pixels width) along the dashed line in (C) and corresponding Gaussian peak fits.
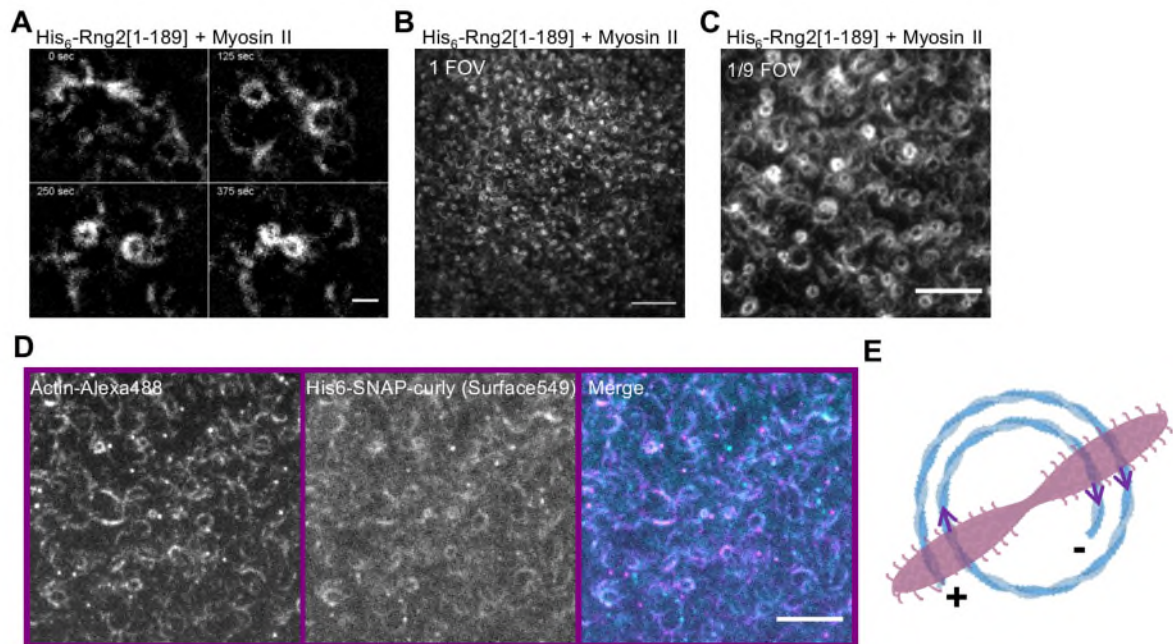
15

Figure 3 - figure supplement 4

524
Figure 3-figure supplement 4

(A) TIRF microscopy image time series showing actin filament (Alexa488) ring formation, translation and contraction driven by myosin II filaments when bound to membrane tethered His$_6$-curly; scale bar: 1 μm.

(B) TIRF microscopy image (representing one field of view) of actin filaments (Alexa488) 20 min after addition of muscle myosin II filaments on His$_6$-curly containing SLBs; scale bar: 10 μm.

(C) TIRF microscopy image (representing one field of view) of actin filaments (Alexa488) 20 min after addition of muscle myosin II filaments on His$_6$-curly containing SLBs; scale bar: 5 μm.

(D) Dual color TIRF microscopy image of actin filaments (Alexa488, magenta) bound to membrane tethered fluorescently labelled His$_6$-SNAP-curly (Surface549, cyan) 20 min after addition of myosin II filaments; scale bar 5 μm.

(E) Model representing how myosin II filaments could drive the contraction of curly formed actin rings.

16

561 Since Rng2 belongs to the IQGAP protein family, we tested the N-terminal hexa-histidine
562 tagged fragments of the IQGAP proteins Iqg1[1-330] (*S. cerevisiae*) and IQGAP1[1-678] (*H.*
563 *sapiens*) and found that the bending of actin filaments was conserved ($C_{S.C.}$ = 1.1 ± 0.4 µm^{-1};
564 N = 110; $C_{H.S.}$ = 1.0 ± 0.2 µm^{-1}; N = 290) (Figure 4 A-C). Comparison of the available crystal
565 structures of *H. sapiens* IQGAP1[28-190] with *S. pombe* Rng2[32-190] indicates a high
566 similarity between the two (Figure 4-figure supplement 1).
567
568 Finally, to test the effect of curly on the actin cortex in cells, we expressed curly-EGFP in the
569 mammalian cell lines HEK293T and RPE-1, which resulted in obvious changes in the actin
570 cortex architecture with prominent occurrence of curved actin filaments and bundles with
571 curvatures of $C_{HEK293T}$ = 2.3 ± 0.4 µm^{-1} (N = 91 from 14 cells), and C_{RPE-1} = 1.9 ± 0.6 µm^{-1} (N
572 = 113 from 11 cells) (Figure 4D-F). Co-expression with LifeAct-mCherry confirmed that
573 EGFP-Curly bound to actin filaments in cells (Figure 4-figure supplement 2). These
574 experiments established that curly could instructively reorganize actin filaments / networks
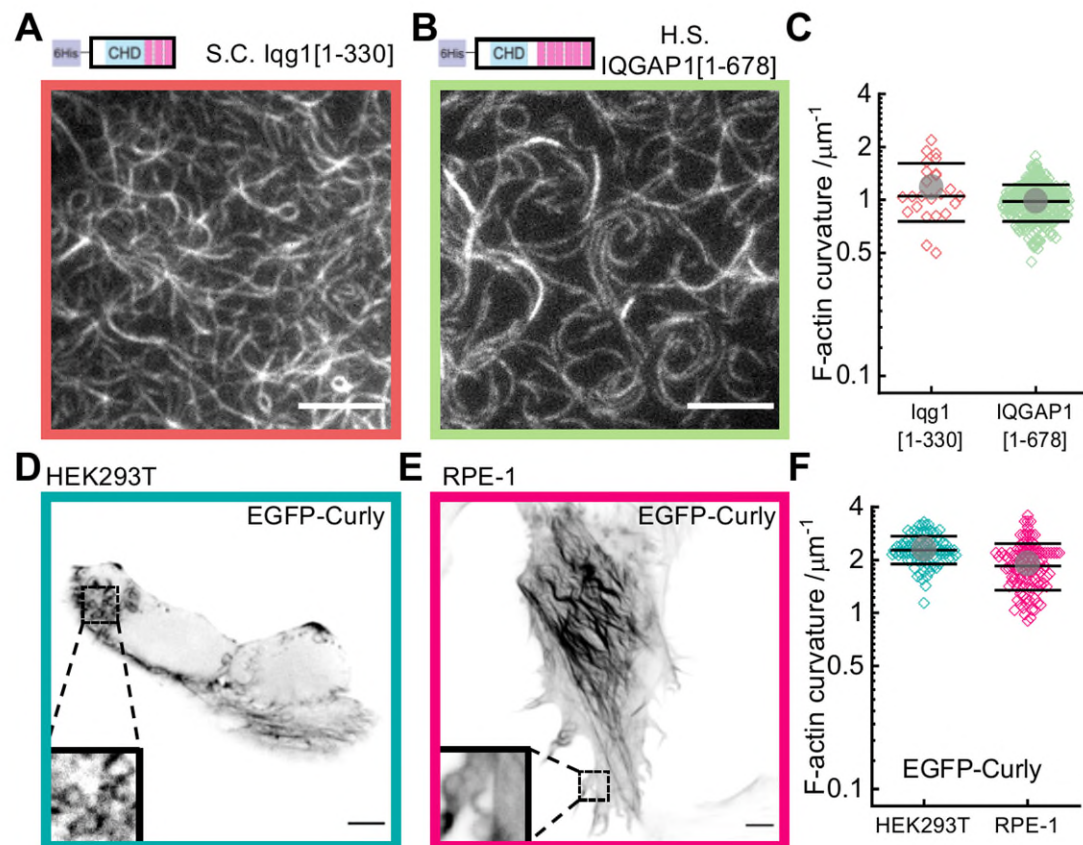575 into curved structures and rings.
576
577
578
579
580
581
582
583
584
585
586
587
588
589
590
591
592
593
594
595
596
597
598
599
600
601
602
603
604
605
606
607
608
609
610
611
612
613
614
615
616
617
618

17

Figure 4

619
620
621 **Figure 4 – Curly effect is conserved among species and it can foster actin bending in**
622 **mammalian cells**
623   (A) TIRF microscopy image of actin filaments (Alexa488) bound to membrane tethered
624   His6-Iqg1[1-330] (*S. cerevisiae*); scale bar: 5 μm.
625   (B) TIRF microscopy image of actin filaments (Alexa488) bound to membrane tethered
626   His6-IQGAP1[1-678] (*H. sapiens*); scale bar: 5 μm.
627   (C) Curvature measurements of actin filament rings and curved segments; shown are the
628   individual data points and their mean ± s.d.; Iqg1[1-330] (orange): N = 167 from 12 field
629   of views of 4 individual experiments; IQGAP1[1-678] (green): N = 407 from 20 field of
630   views of 3 individual experiments.
631   (D) Confocal microscopy image (average intensity projection of the basal cell section) of a
632   HEK293T cell transfected with EGFP-Curly, inlet shows zoom of dashed box; scale bar: 5
633   μm.
634   (E) Confocal microscopy image (average intensity projection of the basal cell section) of a
635   REP-1 cell transfected with EGFP-Curly, inlet shows zoom of dashed box; scale bar: 5
636   μm.
637   (F) Curvature measurements of actin filament rings and curved segments found in EGFP-
638   Curly expressing cells; shown are the individual data points and their mean ± s.d.;
639   HEK293T (teal): N 91 from 14 cells of 2 individual experiments; REP-1 (fuchsia): N =
640   113 from 11 cells of 2 individual experiments.
641
642
643
644
645
646
647
648

18

Figure 4 – figure supplement 1

Human IQGAP1

IQGAP1 (28-190)
PDB: 3i6X

C

N

■ IQGAP1-N (28-43)
■ IQGAP1-CHD (44-159)
■ IQGAP1-Curly (160-190)
● IQGAP1-linker (165-172)

S.pombe Rng2

Rng2 (32-190)
PDB: 1P2X

C

N

■ Rng2-N (32-40)
■ Rng2-CHD (41-147)
■ Rng2-Curly (148-190)
● Rng2-linker (154-160)

Superimpose

IQGAP1 (33-190)
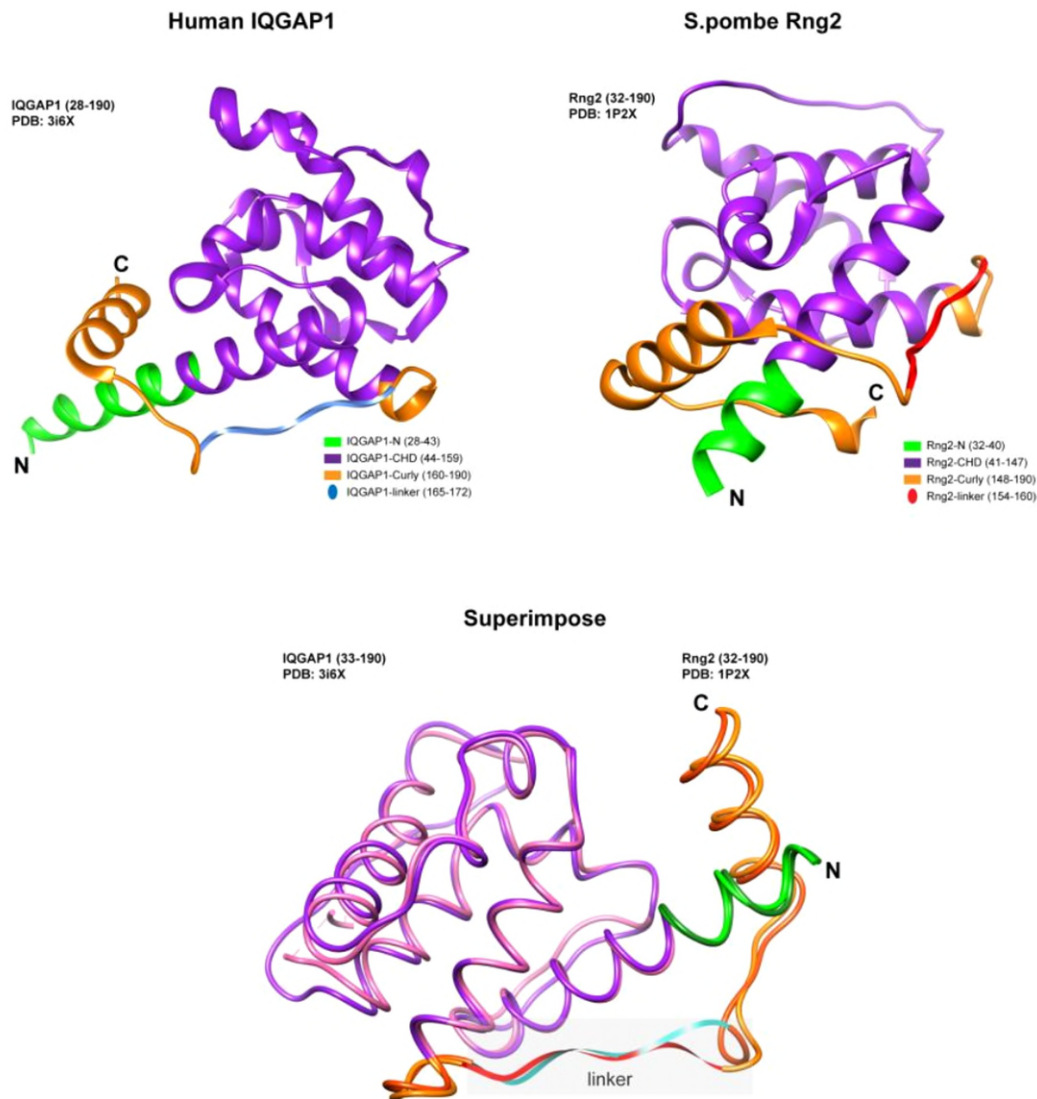PDB: 3i6X

Rng2 (32-190)
PDB: 1P2X

C

N

linker

649
650 **Figure 4-figure supplement 1**
651 Depiction of structure predictions and overlay of *H. sapiens* IQGAP1[28-190] and *S. pombe*
652 Rng2[32-190] indicating the strong similarity between the linker regions of both proteins that
653 are thought to be important for actin bending.
654
655
656
657
658
659
660
661
662
663
664
665
666
667
668
669
670

19

Figure 4 – figure supplement 2

A

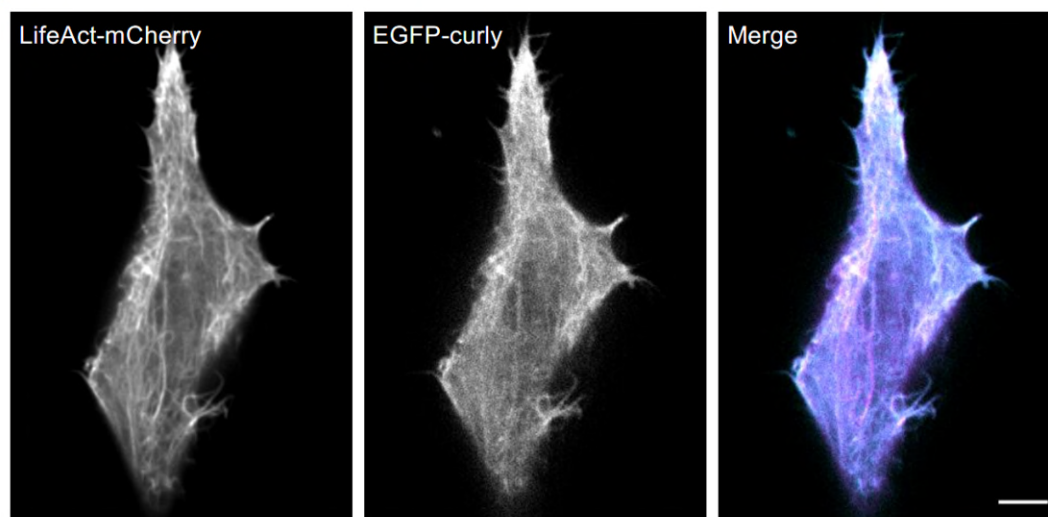
LifeAct-mCherry   EGFP-curly   Merge

671
672
673 **Figure 4-figure supplement 2**
674 Dual color confocal microscopy image (average intensity projection of the basal cell section) of a
675 HEK293T cell transfected with LifeAct-mCherry (magenta) and EGFP-Curly (cyan); scale bar: 5
676 µm.
677
678
679
680
681
682
683
684
685
686
687
688
689
690
691
692
693
694
695
696
697
698
699
700
701
702
703
704
705
706
707
708

Discussion

Our results show that the N-terminal CHD of IQGAP proteins induces actin filament bending when tethered to lipid membranes, which constitutes a new type of actin binding protein and could be an important link between actin and membrane geometries. Recently, Uyeda and colleagues reported that curly (Rng2[1-189]) in solution can induce kinks at random locations of the actin filament (Hayakawa et al., 2020). This together with our results indicates that curly that is constrained to a lipid membrane, would bind asymmetrically to actin filaments leading to a succession of kinks towards the same direction leading to curling of the actin filaments into rings in the plane of the lipid membrane. With an estimated His_6-Curly surface density on SLBs of 5000 μm^{-2} (Köster et al., 2016; Nye & Groves, 2008) the approximated curly to actin ratio would be 1:7 or higher. The mobility of curly on the SLB allowing accumulation under actin filaments was important for continuous actin filament bending into rings as glass-immobilized curly failed to generate rings. In line with this, curly in solution, i.e. in the absence of a substrate providing confinement, did not lead to persistent bending of actin filaments (Hayakawa et al., 2020). Interestingly, individual transient kinks of an average angle of 37° ± 8° could be observed during actin filament binding to curly, but it remained unclear whether this is caused by binding of single or multiple proteins. Based on the data of the Utrophin-CHD actin binding sites (Kumari et al., 2020) together with the newly identified actin binding region withing Rng2[150-189], the local change of the actin filament structure induced by curly could be similar to the effect of cofilin (Narita, 2020) allowing the formation of actin rings with curvatures that would be energetically unfavorable given the actin filament persistence length of 10 μm (De La Cruz & Gardel, 2015). The increased flexibility of actin filaments is highlighted by the fact that addition of rabbit muscle myosin II filaments resulted in actin ring constriction without any evidence for filament rupture up to curvatures of 6.3 μm^{-1} which is much higher than expected for actin alone (Taylor et al., 2000). This mechanism of actin ring formation stands out as it bends individual actin filaments in contrast to other reported systems that generate actin rings made of bundles of actin filaments (Litschel et al., 2020; Mavrakis et al., 2014; Mishra et al., 2013; Way et al., 1995).

In case of *S. pombe* cytokinetic ring formation, Rng2 is localized at the plasma membrane by interaction with Mid1 via its C-terminal RAS-GAP and GRD domains (Almonacid et al., 2011; Padmanabhan et al., 2011) leaving the N-terminal CHD facing the cytoplasm and allowing interaction with actin filaments. Formin based polymerization of actin filaments is essential for cytokinetic ring formation and binding of the tropomyosin Cdc8 supports myosin driven cytokinetic ring contraction. Our work recapitulates that this minimal set of proteins can indeed generate and stabilize actin filaments of the right curvature to form the cytokinetic ring along the short axis of *S. pombe*. Even though electron microscopy data of the cytokinetic ring does not provide clear evidence of bent actin filaments (Swulius et al., 2018), this mechanism could work together with other processes such as cross-linkers ensuring the binding of fresh actin filaments along existing ones (Li & Munro, 2020) to drive robust formation of cytokinetic rings.

Highly bent actin filament structures are most likely important for many cellular structures such as axons (Vassilopoulos et al., 2019; Xu et al., 2013) and mitochondrial actin cages (Kruppa et al., 2018), but the molecular mechanisms leading to their formation are still poorly understood. Future work could provide insights whether curly plays a role in actin ring formation in axons and around mitochondria. In addition, our system of membrane bound curly, actin filaments, and myosin II filaments constitutes a minimalistic system for actin ring formation and constriction and could be used in future to design synthetic dividing vesicles and further exiting active membrane-cortex systems.

Materials and Methods:

Cloning and Protein purification

S. pombe Rng2 fragments, Fim1, Cdc12 (FH1-FH2) and S. cerevisiae Iqg1 were amplified from cDNA library and genomic DNA respectively. Amplified fragments were cloned into pET (6His) and pGEX (GST) based vectors using Gibson cloning method (NEB builder, E5520S). Plasmids used in this study is listed in Table S1.

All protein expression plasmids were transformed into E.coli BL21-(DE3). Single colony was inoculated in 20 ml of LB media supplemented with appropriate antibiotic (pET-Kanamycin; pGEX-Ampicillin). Precultures were grown for ~12-16 h at 36 °C shaking at 200 r.p.m. Cells were diluted to OD600 of 0.1 a.u. in 500 ml of LB with antibiotics and protein expression was induced with 0.25 mM isopropyl β-D-1-thiogalactopyranoside (IPTG). Protein was expressed for 3-4 h at 30 °C shaking at 200 r.p.m. unless otherwise noted. After induction cell pellets were collected and spun down at 7,000 r.p.m for 20 minutes after induction at 4 °C. Media was aspirated and pellets were washed once with cold phosphate buffered saline (PBS) with 1mM phenylmethylsulfonyl fluoride (PMSF), and pellets were stored at −80 °C.

His tagged protein (His6-Rng2, Igg1 and Iqgap1) purification: Cell pellets for purification were thawed on ice for 10 minutes. The pellets were resuspended in 10 ml of lysis buffer for sonication (50 mM Napi pH 7.6, 200 mM NaCl, 10mM Imidazole pH 7.5, 0.5 mM EDTA, 1 mM DTT, 1 mg/ ml lysozyme, and complete mini-EDTA-Free protease inhibitor cocktail tablets) and incubated on ice for 20 min, followed by sonication (8 cycles, 15 sec pulse). The lysates were centrifuged at 14000 r.p.m, 30 min, 4 °C and the clarified lysate was transferred to a 15-ml tube. The 400 µl slurry of HisPur™ Ni-NTA agarose resin (cat. no. 88221, Thermo fisher) was washed with wash buffer (5x) (50 mM Napi (pH 7.6), 300 mM NaCl, 30mM Imidazole pH 7, 0.5 mM EDTA and 1 mM DTT) before the lysate was added. The clarified lysate was added to the washed Ni-NTA resin and incubated for 2h at 4 °C. After incubation with NiNTA resin, beads were washed with wash buffer 6-8 times in BIO-RAD prepacked column. Protein was eluted using Ni-NTA elution buffer (50 mM NaPi pH 7.6, 300 mM NaCl, 0.5 mM EDTA, 1 mM DTT and 500 mM imidazole) and 300 µl elutions were collected in a clean Eppendorf tubes. Each fraction was assessed by SDS–polyacrylamide gel electrophoresis (SDS–PAGE). The eluates (E1-E3) were pooled, concentrated and buffer exchanged into the protein storage buffer (50 mM Tris-HCl pH 7.4, 150 mM NaCl, 1 mM DTT and 10% glycerol) using a PD MiniTrap G-25 sephadex columns (GE Healthcare) and the protein was stored at −80 °C. The protein concentration was estimated by UV280 and by comparing known quantities of BSA standards on an SDS–PAGE gel.

GST tagged protein (GST-Fim1) purification: Cell pellets for purification were thawed on ice for 10 minutes. The pellets were resuspended in 10 ml of lysis buffer for sonication (PBS, 0.5 mM EDTA, 1 mM DTT, 1 mg/ ml lysozyme, and complete mini-EDTA-Free protease inhibitor cocktail tablets) and incubated on ice for 20 min, followed by sonication (10 cycles, 15 sec pulse). After sonication cell lysate was incubated with 0.5% Triton-X-100 for 20 minutes on ice. The lysates were centrifuged at 22000xg, 30 min, 4 °C and the clarified lysate was transferred to a 15-ml tube. The 400 µl slurry of glutathione sepharose-4B resin (cat. no. GE17-0756-01, GE) was washed with wash buffer (5x) (PBS, 0.5 mM EDTA and 1 mM DTT) before the lysate was added. The clarified lysate was added to the washed glutathione sepaharose resin and incubated for 2-3h at 4 °C. After incubation with sepharose resin, beads were washed with wash buffer 6-8 times in poly-prep chromatography columns (BIO-RAD laboratories Inc). Protein was eluted using GST elution buffer (50 mM Tris-HCl pH8.0 and 10 mM glutathione). Purified protein sample was quantified and stored in the storage buffer as described above in the previous section.

Acetylation mimicking version of tropomyosin (ASCdc8) was expressed in BL21-DE3 and protein was purified by boiling and precipitation method as described earlier (Palani et al., 2019; Skoumpla et al., 2007). Purified tropomyosin was dialyzed against the storage buffer

22

824   (50 mM NaCl, 10 mM imidazole, pH 7.5, and 1 mM DTT), flash frozen in liquid N2 and
825   stored at -80 °C.
826
827   SNAP labelling (SNAP-Surface® 549, S9112S, NEB) of capping protein-beta and Rng2 1-
828   189 was performed as per the manufactures protocol.
829
830   **Co-sedimentation assay and Immunoblot**
831
832   Co-sedimentation assays were performed at 25°C by mixing 3 µM actin with different Rng2
833   fragments, ScIqg1(1-330) and Hs IGAP1 (1-678), and then spun at 100,000 g (high speed)
834   for 20 min at 25°C. Equal volumes of supernatant and pellet were separated by 12% SDS-
835   PAGE gel and stained with Coomassie blue (SimplyBlueStain, Invitrogen) or immunoblotted.
836   For western analysis, equal volumes of each sample were diluted in 1 × Laemmli buffer (Bio-
837   Rad). Samples were run on a hand cast 10-well 12% acrylamide gels (Bio-Rad), transferred
838   onto nitro cellulose membranes and blotted with 1:1000 Anti-His-HRP (6xHis Epitope TAG,
839   Cat. no. sc-8036 HRP, Santa Cruz Inc) and 1:500 anti-actin-HRP (cat. no. sc-47778 HRP,
840   Santa Cruz Inc). Signal was detected by enhanced chemiluminescence (Clarity western
841   ECL, Bio-Rad) imaged on a ChemiDoc MP (Bio-Rad).
842
843   **Mammalian expression**
844
845   S. pombe Rng2 fragment (1-189) was cloned into pCDNA3.1-eGFP using gibson cloning
846   method. HEK293 and RPE1 cells were transiently transfected with pCDNA3 containing
847   SpRng2 (1-189) using Lipofectamine 2000 (cat. no. 11668019, Life Technologies) following
848   manufacturer's instructions. Cells were transfected at ~70% confluency for 24 h before the
849   experiments. For each imaging condition, 500,000 cells were transfected with 1 µg of DNA.
850   Cells were seeded and imaged on µ-Dish 35 mm (cat. no. 81156, IBIDI). Before imaging, the
851   culture medium was replaced with phenol red–free DMEM (Opti-MEM, cat. no. 31985062,
852   Life Technologies). Images were taken using spinning disk microscope with a 100× Apo
853   objective, NA 1.4.
854
855   **In vitro assay and Total Internal Reflection Fluorescence (TIRF) microscopy**
856
857   *Supported Lipid Bilayer and Experimental Chamber Preparation*
858   The sample preparation, experimental conditions and lipid composition were similar to the
859   ones described in previous work [Koester et al, 2016]. Glass coverslips (#1.5 borosilicate,
860   Menzel, cat. no. 11348503, Fisher Scientific) for SLB formation were cleaned with
861   Hellmanex III (Hellma Analytics, cat. No. Z805939, Merck) following the manufacturer's
862   instructions followed by thorough rinses with EtOH and MilliQ water and blow dried with N2
863   gas. For the experimental chamber, 0.2 ml PCR tubes (cat. no. I1402-8100, Starlab) were
864   cut to remove the lid and conical bottom part. The remaining ring was stuck to the cleaned
865   glass using UV glue (cat. no. NOA88, Norland Products) and three minutes curing by
866   intense UV light at 265 nm (UV Stratalinker 2400, Stratagene). Freshly cleaned and
867   assembled chambers were directly used for experiments.
868   Supported lipid bilayers (SLB) containing 98% DOPC (cat. no. 850375, Avanti Polar Lipids)
869   and 2% DGS-NTA(Ni2+) (cat. no. 790404, Avanti Polar Lipids) lipids were formed by fusion
870   of small uni-lamellar vesicles (SUV) that were prepared by lipid extrusion using a membrane
871   with 100 nm pore size (cat. no. 610000, Avanti Polar Lipids). SLBs were formed by addition
872   of 10 µl of SUV mix (at 4 mM lipid concentration) to chambers filled with 90 µl KMEH (50 mM
873   KCl, 2 mM MgCl$_2$, 1 mM EGTA, 20 mM HEPES, pH 7.2) and incubation for 30 min. Prior to
874   addition of other proteins, the SLBs were washed 10 times by buffer exchange (always
875   leaving 20 µl on top of the SLB to avoid damage by drying). We tested the formation of lipid
876   bilayers and the mobility of lipids in control samples by following the recovery of
877   fluorescence signal after photobleaching of hexa-histidine tagged GFP (His$_6$-GFP) as
878   described in (Köster et al., 2016).
879
880   *Actin filament polymerization and tethering to SLBs*

23

881 Actin was purified from muscle acetone powder form rabbit (cat. no. M6890, Merck) and
882 labelled with Alexa488-maleimide (cat. no. A10254, Thermo Fisher) following standard
883 protocols (Köster et al., 2016; Pardee & Spudich, 1982).
884 In a typical experiment, actin filaments were polymerized in parallel to SLB formation to
885 ensure that all components of the experiment were freshly assembled before starting
886 imaging. First $10\%_{vol}$ of 10x ME buffer (100 mM $MgCl_2$, 20 mM EGTA, pH 7.2) were mixed
887 with unlabeled and labeled G-actin (to a final label ratio of 20%), optionally supplemented
888 with labelled capping protein in G-actin buffer (1 mM $CaCl_2$, 0.2mM ATP, 2mM Tris, 0.5 mM
889 TCEP-HCl, pH 7.2) to a final G-actin concentration of 10 µM and incubated for 2 min to
890 replace G-actin bound Ca^{2+} ions with Mg^{2+} ions. Polymerization of actin filaments was
891 induced by addition of an equal amount of 2x KMEH buffer supplemented with 2 mM Mg-
892 ATP bringing the G-actin concentration to 5 µM. After 30 min incubation time, actin filaments
893 were added to the SLBs using blunt-cut pipette tips at a corresponding G-actin concentration
894 of 100 nM (to ensure a homogenous mix of actin filaments, 2 µl of actin filament solution was
895 mixed in 18 µl KMEH and then added to the SLB containing 80 µl KMEH). After 10 min of
896 incubation, His_6-Curly or other variants of histidine-tagged actin binding proteins at a final
897 concentration of 10 nM were added and a short time after (1 - 5 min) binding of actin to the
898 SLB could be observed using TIRF microscopy.

900 In experiments with formin, the SLB was first incubated with 10 nM His_6-SpCdc12(FH1-FH2)
901 and 10 nM His_6-Curly for 20 min, then washed twice with KMEH. During the incubation time,
902 $10\%_{vol}$ of 10x ME buffer was mixed with unlabeled and labeled G-actin at 4 µM (final label
903 ratio of 20%) together with 5 µM profilin and incubated for 5 min prior to addition to the SLB
904 and imaging with TIRF microscopy.

906 In experiments with tropomyosin or fimbrin, actin filaments ($C_{G-actin}$ = 1 µM) were incubated
907 with tropomyosin at a 1:3 protein concentration ratio or with fimbrin at a 3:2 protein
908 concentration ratio for 15 min prior to addition to the SLB (Palani et al., 2019).

910 In experiments with muscle myosin II filaments, we prepared muscle myosin II filaments by
911 diluting the stock of muscle myosin II proteins (rabbit, m. psoas, cat. no. 8326-01, Hypermol)
912 (C_{myoII} = 20 µM; 500mM KCl, 1mM EDTA, 1 mM DTT, 10 mM HEPES, pH 7.0) 10-times with
913 MilliQ water to drop the KCl concentration to 50 mM and incubated for 5 min to ensure
914 myosin filament formation. Myosin II filaments were further diluted in KMEH to 200 nM and
915 added to the actin filaments bound to the SLB by His_6-Curly by replacing 1/10 of the sample
916 buffer with the myosin II filament solution and supplemented with 0.1 mM Mg-ATP as well as
917 a mix of 1 mM Trolox (cat. no. 648471, Merck), 2 mM protocatechuic acid (cat. no.
918 03930590, Merck) and 0.1 µM protocatechuate 3,4-dioxygenase (cat. no. P8279, Merck) to
919 minimize photobleaching. To summarize, the final buffer composition was 50mM KCl, 2mM
920 $MgCl_2$, 1mM EGTA, 20mM HEPES, 0.1mM ATP, 1 mM Trolox, 2 mM protocatechuic acid
921 and 0.1 µM protocatechuate 3,4-dioxygenase at pH 7.2 containing actin filaments ($C_{G-actin}$ =
922 100 nM) and myosin II filaments (C_{myoII} = 20 nM). It was important to keep the pH at 7.2, as
923 changes in pH would affect motor activity. As reported earlier, myosin filaments started to
924 show actin network remodeling activity after about 10-15 min of incubation (Köster et al.,
925 2016; Mosby et al., 2020).

927 *TIRF microscopy*
928 Images were acquired using a Nikon Eclipse Ti-E/B microscope equipped with perfect focus
929 system, a Ti-E TIRF illuminator (CW laser lines: 488nm, 561nm and 640nm) and a Zyla
930 sCMOS 4.2 camera (Andor, Oxford Instruments, UK) controlled by Andor iQ3 software
931 (https://andor.oxinst.com/products/iq-live-cell-imaging-software/).

933 **Image analysis**
934 Images were analyzed using ImageJ (http://imagej.nih.gov/ij).
935 Curvature was measured by fitting ellipses to match the actin filament contour by hand,
936 while measuring first fully formed rings before curved actin filament segments and by going
937 from the highest curvatures down to lower curvatures in each image with a cut off for

24

938 measurements at curvatures smaller than 0.1 μm^{-1} or at 30-40 measurements per image
939 (see examples in Figure 1 – figure supplement 1D; Figure 1-figure supplement 2B).
940 To measure the angle of kinks in individual actin filaments, cropped images of individual
941 actin filaments were processed with a Sobel filter (part of the Mosaic suit for ImageJ,
942 http://mosaic.mpi-cbg.de/?q=downloads/imageJ) to highlight the actin filament center, and
943 the angles were measured manually with the ImageJ angle tool.
944 The actin ring contraction rate upon myosin II filament action was measured by generating
945 kymographs based on a line (3 pixels width) dividing the ring into two equal halves.
946
Data plotting and statistics
948 Graphs were generated using OriginPro (version 2019b, OriginLab, USA). Plots depict
949 individual data points, mean (circle), median (central line) and standard deviation (top and
950 bottom lines).
951

958

Competing Interests
960 The authors have no competing interests to declare.
961

962

Video captions
964

965 Video 1: TIRF microscopy image sequence of actin filaments (Alexa488) landing on His_6-
966 curly decorated SLBs; scale bar: 5 µm.
967

968 Video 2: Example image sequence of an actin filament (Alexa488) bound to a His_6-curly
969 decorated SLB displaying individual bending events after processing the image sequence
970 with a Sobel filter to highlight the shape of the actin filament (the unprocessed images are
971 shown in Figure 2-figure supplement 2); scale bar: 1 µm.
972

973 Video 3: Example image sequence of an actin filament (Alexa488, gray) with the plus end
974 labelled by capping protein (SNAP647, yellow) landing on a His_6-curly decorated SLB; scale
975 bar: 1 µm.
976

977 Video 4: Example image sequence of an actin filament (Alexa488, gray) with the plus end
978 labelled by capping protein (SNAP647, cyan) landing on a curly-His_6 decorated SLB; scale
979 bar: 1 µm.
980

981 Video 5: Example image sequences of actin filaments (Alexa488) polymerized by SLB
982 tethered formin in the presence of His_6-curly bound to the SLB; scale bar 1 µm.
983

984 Video 6: Example image sequences of actin filaments (Alexa488) decorated with
985 tropomyosin binding to membrane tethered His_6-curly; scale bar: 1 µm.
986

987 Video 7: Example image sequence showing formation, translation, and contraction of actin
988 filament (Alexa488) rings on membrane tethered His_6-curly after the addition of muscle
989 myosin II filaments; scale bar: 1 µm.
990

991 Video 8: Example image sequences of actin filament (Alexa488) ring contraction on
992 membrane tethered His_6-curly after the addition of muscle myosin II filaments; scale bar: 1
993 µm.
994

995

25

Table 1: Plasmids used in this study

996
997
998
999
1000
1001

pET28C-6HIS-Rng2(1-189)	pSPW153
pET28C-6HIS-Rng2(1-250)	pSPW155
pET28C-6HIS-Rng2(1-300)	pSPW113
pET28C-6HIS-Rng2(1-147)	pSPW167
pET28C-6HIS-Rng2(41-147)	pSPW169
pET28C-6HIS-Rng2 (41-189)	pSPW187
pET28C-6HIS-Rng2 (41-250)	pSPW189
pET28C-6HIS-Rng2 (41-300)	pSPW191
pETMCN-Rng2(1-189)-C-6HIS	pSPW288
pETMCN-Rng2(1-250)-C-6HIS	pSPW290
pETMCN-Rng2(1-300)-C-6HIS	pSPW291
pET28C-6HIS-Rng2(1-189; Δ154-160)	pSPW297
pET28C-6HIS-Rng2(1-300; Δ154-160)	pSPW299
pET28C-6HIS-Curly100 (150-250)	pSPW284
pET23a-10HIS-SNAP-Rng2-CHD (1-300)	pSPW195
pET28C-6HIS-ScIqg1 (1-330)	pSPW200
pET28C-6HIS-HsIQGAP1 (1-678)	pSPW293
pCDNA3-EGFP-GSGG-Rng2(1-189)	pSPW620
pET-3d-6HIS-SNAP-tagged β1 subunit and untagged α1 subunits of chicken CapZ	Addgene: 69948 Bombardier et al., 2015
pET28C-6HIS-Cdc12 (740-1391)	pSPW123
pETMCN-AScdc8	pSPW036
pGEX4T1-GST-Fim1	pSPW114
pET23a-10HIS-SNAP-Ezrin-ABD	pSPW151
pGEX-alpha actinin4 (acnt4)	Gift from L. Blanchoin's lab

1002
1003
1004
1005
1006
1007
1008
1009
1010
1011

References

Almonacid, M., Celton-Morizur, S., Jakubowski, J. L., Dingli, F., Loew, D., Mayeux, A., Chen, J. S., Gould, K. L., Clifford, D. M., & Paoletti, A. (2011). Temporal control of contractile ring assembly by Plo1 regulation of myosin II recruitment by Mid1/anillin. *Current Biology*, *21*(6), 473–479. https://doi.org/10.1016/j.cub.2011.02.003

Bieling, P., Li, T.-D., Weichsel, J., McGorty, R., Jreij, P., Huang, B., Fletcher, D. A., & Mullins, R. D. (2016). Force Feedback Controls Motor Activity and Mechanical Properties of Self-Assembling Branched Actin Networks. *Cell*, *164*(1–2), 115–127. https://doi.org/10.1016/j.cell.2015.11.057

Briggs, M. W., & Sacks, D. B. (2003). IQGAP proteins are integral components of cytoskeletal regulation. *EMBO Reports*, *4*(6), 571–574. https://doi.org/10.1038/sj.embor.embor867

De La Cruz, E. M., & Gardel, M. L. (2015). Actin mechanics and fragmentation. *Journal of Biological Chemistry*, *290*(28), 17137–17144. https://doi.org/10.1074/jbc.R115.636472

Eng, K., Naqvi, N. I., Wong, K. C. Y., & Balasubramanian, M. K. (1998). Rng2p, a protein required for cytokinesis in fission yeast, is a component of the actomyosin ring and the spindle pole body. *Current Biology*, *8*(11), 611–621. https://doi.org/10.1016/S0960-9822(98)70248-9

Epp, J. A., & Chant, J. (1997). An IQGAP-related protein controls actin-ring formation and cytokinesis in yeast. *Current Biology*, *7*(12), 921–929. https://doi.org/10.1016/S0960-9822(06)00411-8

Hayakawa, Y., Takaine, M., Imai, T., Yamada, M., Hirose, K., Tokuraku, K., Ngo, K. X., Kodera, N., Numata, O., Nakano, K., & Uyeda, T. Q. P. (2020). Actin binding domain of Rng2 strongly inhibits actin movement on myosin II HMM through structural changes of actin filaments. *BioarXiv*.

Köster, D. V., Husain, K., Iljazi, E., Bhat, A., Bieling, P., Mullins, R. D., Rao, M., & Mayor, S. (2016). Actomyosin dynamics drive local membrane component organization in an in vitro active composite layer. *Proceedings of the National Academy of Sciences*, *113*(12), E1645–E1654. https://doi.org/10.1073/pnas.1514030113

Kruppa, A. J., Kishi-Itakura, C., Masters, T. A., Rorbach, J. E., Grice, G. L., Kendrick-Jones, J., Nathan, J. A., Minczuk, M., & Buss, F. (2018). Myosin VI-Dependent Actin Cages Encapsulate Parkin-Positive Damaged Mitochondria. *Developmental Cell*, *44*(4), 484-499.e6. https://doi.org/10.1016/j.devcel.2018.01.007

Kučera, O., Janda, D., Siahaan, V., Dijkstra, S. H., Pilátová, E., Zatecka, E., Diez, S., Braun, M., & Lansky, Z. (2020). Anillin propels myosin-independent constriction of actin rings. *BioRxiv*, 1–27. https://doi.org/10.1101/2020.01.22.915256

Kumari, A., Kesarwani, S., Javoor, M. G., Vinothkumar, K. R., & Sirajuddin, M. (2020). Structural insights into actin filament recognition by commonly used cellular actin markers. *The EMBO Journal*, 846337. https://doi.org/10.15252/embj.2019104006

Laplante, C., Huang, F., Tebbs, I. R., Bewersdorf, J., & Pollard, T. D. (2016). Molecular organization of cytokinesis nodes and contractile rings by super-resolution fluorescence microscopy of live fission yeast. *Proceedings of the National Academy of Sciences*, *113*(40), E5876–E5885. https://doi.org/10.1073/pnas.1608252113

Laporte, D., Coffman, V. C., Lee, I. J., & Wu, J. Q. (2011). Assembly and architecture of precursor nodes during fission yeast cytokinesis. *Journal of Cell Biology*, *192*(6), 1005–1021. https://doi.org/10.1083/jcb.201008171

Li, Y., & Munro, E. (2020). Existing actin filaments orient new filament growth to provide structural memory of filament alignment during cytokinesis. *BioRxiv*. https://doi.org/10.1101/2020.04.13.039586

Litschel, T., Kelley, C. F., Holz, D., Koudehi, M. A., Vogel, S. K., Burbaum, L., Mizuno, N., Vavylonis, D., & Schwille, P. (2020). Reconstitution of contractile actomyosin rings in vesicles. *BioRxiv*. https://doi.org/10.1101/2020.06.30.180901

Mavrakis, M., Azou-Gros, Y., Tsai, F.-C., Alvarado, J., Bertin, A., Iv, F., Kress, A., Brasselet, S., Koenderink, G. H., & Lecuit, T. (2014). Septins promote F-actin ring formation by crosslinking actin filaments into curved bundles. *Nature Cell Biology*, *16*(4), 322–334. https://doi.org/10.1038/ncb2921

Mishra, M., Kashiwazaki, J., Takagi, T., Srinivasan, R., Huang, Y., Balasubramanian, M. K.,

27

& Mabuchi, I. (2013). In vitro contraction of cytokinetic ring depends on myosin II but not on actin dynamics. *Nature Cell Biology*, *15*(7), 853–859. https://doi.org/10.1038/ncb2781

Mosby, L. S., Hundt, N., Young, G., Fineberg, A., Polin, M., Mayor, S., Kukura, P., & Köster, D. V. (2020). Myosin II Filament Dynamics in Actin Networks Revealed with Interferometric Scattering Microscopy. *Biophysical Journal*, *118*(8), 1946–1957. https://doi.org/10.1016/j.bpj.2020.02.025

Murrell, M. P., & Gardel, M. L. (2012). F-actin buckling coordinates contractility and severing in a biomimetic actomyosin cortex. *Proceedings of the National Academy of Sciences of the United States of America*, *19*. https://doi.org/10.1073/pnas.1214753109

Narita, A. (2020). ADF/cofilin regulation from a structural viewpoint. *Journal of Muscle Research and Cell Motility*, *41*(1), 141–151. https://doi.org/10.1007/s10974-019-09546-6

Nye, J. A., & Groves, J. T. (2008). Kinetic control of histidine-tagged protein surface density on supported lipid bilayers. *Langmuir : The ACS Journal of Surfaces and Colloids*, *24*(8), 4145–4149. https://doi.org/10.1021/la703788h

Padmanabhan, A., Bakka, K., Sevugan, M., Naqvi, N. I., D'Souza, V., Tang, X., Mishra, M., & Balasubramanian, M. K. (2011). IQGAP-related Rng2p organizes cortical nodes and ensures position of cell division in fission yeast. *Current Biology*, *21*(6), 467–472. https://doi.org/10.1016/j.cub.2011.01.059

Palani, S., Köster, D. V., Hatano, T., Kamnev, A., Kanamaru, T., Brooker, H. R., Hernandez-Fernaud, J. R., Jones, A. M. E., Millar, J. B. A., Mulvihill, D. P., & Balasubramanian, M. K. (2019). Phosphoregulation of tropomyosin is crucial for actin cable turnover and division site placement. *The Journal of Cell Biology*, jcb.201809089. https://doi.org/10.1083/jcb.201809089

Pardee, J. D., & Spudich, J. A. (1982). Purification of muscle actin. *Methods in Cell Biology*, *24*, 271–289. http://www.ncbi.nlm.nih.gov/pubmed/7098993

Skau, C. T., & Kovar, D. R. (2010). Fimbrin and tropomyosin competition regulates endocytosis and cytokinesis kinetics in fission yeast. *Current Biology*, *20*(16), 1415–1422. https://doi.org/10.1016/j.cub.2010.06.020

Skoumpla, K., Coulton, A. T., Lehman, W., Geeves, M. A., & Mulvihill, D. P. (2007). Acetylation regulates tropomyosin function in the fission yeast Schizosaccharomyces pombe. *Journal of Cell Science*, *120*(9), 1635–1645. https://doi.org/10.1242/jcs.001115

Swulius, M. T., Nguyen, L. T., Ladinsky, M. S., Ortega, D. R., Aich, S., Mishra, M., & Jensen, G. J. (2018). Structure of the fission yeast actomyosin ring during constriction. *Proceedings of the National Academy of Sciences of the United States of America*, *115*(7), E1455–E1464. https://doi.org/10.1073/pnas.1711218115

Taylor, K. A., Taylor, D. W., & Schachat, F. (2000). Isoforms of α-actinin from cardiac, smooth, and skeletal muscle form polar arrays of actin filaments. *Journal of Cell Biology*, *149*(3), 635–645. https://doi.org/10.1083/jcb.149.3.635

Tebbs, I. R., Pollard, T. D., & D, P. T. (2013). Separate roles of IQGAP Rng2p in forming and constricting the Schizosaccharomyces pombe cytokinetic contractile ring. *Molecular Biology of the Cell*, *24*(12), 1904–1917. https://doi.org/10.1091/mbc.E12-10-0775

Toyoshima, Y. Y., Kron, S. J., & Spudicht, J. A. (1990). The myosin step size: Measurement of the unit displacement per ATP hydrolyzed in an in vitro assay (actin/crossbridge/muscle contraction). In *Proc. Nati. Acad. Sci. USA* (Vol. 87, Issue September).

Vassilopoulos, S., Gibaud, S., Jimenez, A., Caillol, G., & Leterrier, C. (2019). Ultrastructure of the axonal periodic scaffold reveals a braid-like organization of actin rings. *Nature Communications*, *10*(1), 636217. https://doi.org/10.1038/s41467-019-13835-6

Wang, C.-H., Balasubramanian, M. K., & Dokland, T. (2004). Structure, crystal packing and molecular dynamics of the calponin-homology domain of Schizosaccharomyces pombe Rng2. *Acta Crystallographica Section D Biological Crystallography*, *60*(8), 1396–1403. https://doi.org/10.1107/S0907444904012983

Way, M., Sanders, M., Garcia, C., Sakai, J., & Matsudaira, P. (1995). Sequence and domain organization of scruin, an actin-cross-linking protein in the acrosomal process of Limulus sperm. *Journal of Cell Biology*, *128*(1–2), 51–60.

1128   Xu, K., Zhong, G., & Zhuang, X. (2013). Actin, spectrin, and associated proteins form a
1129   periodic cytoskeletal structure in axons. *Science (New York, N.Y.)*, *339*(6118), 452–
1130   456. https://doi.org/10.1126/science.1232251
1131